EES Solar

PAPER

View Article Online
View Journal

Cite this: DOI: 10.1039/d6el00006a

Spacer cation design: promoting vertical orientation in layered perovskites

Alice Scardina, [a] Tobias F. Loeff, [b] Vikram, [b] Nada Mrkyvkova, [cd] Ruggero Sala,[a] Leonardo Marsano,[a] Herlina Arianita Dewi,[e] Riccardo Pallotta, [a] Annalisa Bruno, [efg] Peter Siffalovic, [cd] M. Saiful Islam *[b] and Giulia Grancini *[a]

Low-dimensional hybrid perovskites exhibit strongly anisotropic charge transport due to their layered structure, where organic cations (R) separate n inorganic octahedral slabs. Controlling their vertical crystal orientation is critical for enabling efficient charge extraction in photovoltaic devices, but the underlying mechanism remains poorly understood. Here, we systematically investigate how the interplay between chloride incorporation and aromatic spacer R cation choice dictates the vertical growth and alignment of methylammonium (MA)-based $n = 2$ $R_2MAPb_2(I_{1-x}Cl_x)_7$ perovskites. By combining advanced structural and optoelectronic characterisation with atomistic and machine-learning-accelerated simulations, we identify the fundamental factors governing vertical templating. Chloride incorporation is found to be limited and strongly R cation-dependent, indirectly promoting vertical orientation by altering interfacial energetics rather than by direct lattice substitution. Shorter aromatic cations (2-thiophenemethylammonium, TMA^+, and benzylammonium, BnA^+) induce preferential vertical alignment, yielding uniform morphologies and power conversion efficiencies approaching 8%, which are among the highest reported for purely $n = 2$ perovskites (bandgap of 2 eV). In contrast, longer spacer cation analogues (2-thiopheneethylammonium, TEA^+, and phenethylammonium, PEA^+) favour horizontal growth, producing disordered thin films with a poor photovoltaic response. Our combined experimental–computational insights reveal how the synergy between spacer cation size and chloride-mediated interfacial energetics steers vertical crystallisation, providing rational design principles for wide-bandgap, low-dimensional perovskites with enhanced out-of-plane charge transport and photovoltaic performance.

Received 22nd January 2026
Accepted 28th January 2026

DOI: 10.1039/d6el00006a

rsc.li/EESSolar

Broader context

Low-dimensional hybrid perovskites have recently gained attention as promising materials for stable and tunable wide-bandgap solar cells. Their structural variety offers opportunities to control optoelectronic properties through molecular design, yet implementation in high-performance devices remains limited. Charge transport in these layered systems is inherently anisotropic and depends strongly on the orientation of the inorganic framework. Achieving vertically aligned films, crucial for efficient charge extraction, has proven difficult. Moreover, the impact of the organic spacer cation on crystal growth, structural templating, and charge transport has been explored only marginally, despite its role in defining the layered framework. Here, we demonstrate that rational chemical design—combining chloride incorporation with tailored aromatic ammonium cations—can effectively direct the vertical alignment of low-dimensional hybrid perovskites. By integrating structural, optoelectronic, and computational analyses, we show how the interplay between chloride incorporation, spacer cation size, and growth energetics governs vertical orientation in layered perovskites. This work provides an atomic-scale understanding of the factors that dictate the orientation and charge transport in low-dimensional perovskites. Beyond offering mechanistic insight, this study also highlights the potential of these materials for efficient and compositionally tunable solar cells suitable for next-generation photovoltaic technologies.

[a]Department of Chemistry & INSTM, University of Pavia, Via T. Taramelli 14, 27100 Pavia, Italy. E-mail: giulia.grancini@unipv.it

[b]Department of Materials, University of Oxford, Oxford, OX1 3PH, UK. E-mail: saiful.islam@materials.ox.ac.uk

[c]Center for Advanced Materials Application, Slovak Academy of Sciences, Dúbravská cesta 9, 845 11 Bratislava, Slovakia

[d]Institute of Physics, Slovak Academy of Sciences, Dúbravská cesta 9, 845 11 Bratislava, Slovakia

[e]Energy Research Institute @ NTU, Nanyang Technological University, Research Techno Plaza, 50 Nanyang Drive, 637553, Singapore

[f]School of Materials Science and Engineering, Nanyang Technological University, 50 Nanyang Avenue, 639798, Singapore

[g]School of Physical and Mathematical Science, Nanyang Technological University, 21 Nanyang Link, 637371, Singapore

Introduction

Low-dimensional hybrid perovskites (LD-HPs) have recently emerged as promising wide-bandgap (1.7–2.1 eV) materials enabling high-performance and colour-tuneable photovoltaic (PV) technologies.[1–10] With the general formula $R_2MA_{n-1}Pb_nI_{3n+1}$, where MA is methylammonium, R is a monoammonium spacer organic cation and n represents the number of inorganic layers packed between the organic spacers (defining the dimensionality of the system), a bandgap from 2.6 to 1.7 eV can be achieved by tuning n from 1 to 3.[11–13] Despite the

interesting energetics, there are very few attempts demonstrating efficient working devices with an LD-HP active layer in that bandgap range.[14] This is mainly due to the challenge in both (i) controlling the formation of a phase-pure LD-HP and (ii) directing vertical crystal growth of the LD-HP inorganic backbone.[15,16] Achieving vertical orientation, with inorganic planes perpendicular to the substrate, is essential to enhance charge carrier transport and thus increase overall efficiency when integrated into a sandwiched device; this contrasts with horizontally-oriented thin films, which naturally tend to self-assemble from solution, thereby limiting charge extraction.

The correlation between PV performance and vertical crystalline orientation of LD-HP active layers is currently attracting considerable attention.[17–19] We recently demonstrated that chloride (Cl) incorporation is pivotal for achieving vertically oriented $n = 2$ LD-HP thin films with devices surpassing 10% efficiency.[10] However, this condition alone has proven insufficient for most of the R cations commonly studied in the literature with the intrinsic factors governing vertical templating still poorly understood. Over the years, several fundamental aspects have been investigated and linked to the formation of vertically oriented LD-HP thin films, focusing on (i) dimensionality of the system,[20,21] (ii) mutual templating between different n phases,[22] (iii) crystal nucleation and growth mechanisms,[23] (iv) nature of nucleation sites,[23,24] and (v) preferential orientations established by the R cation.[22] Yet, most of these studies have targeted high-n LD-HPs ($n > 3$), where vertical orientation is more favoured because these materials are structurally closer to three-dimensional (3D)-HPs, owing to the lower fraction of the organic component R.[25,26] So far, however, no studies have reported on the influence of the selected R cation on the crystal orientation of low-n (where $n \leq 3$) LD-HP thin films.

The crucial scientific question is can we understand the key design parameters for promoting LD-HP vertical alignment in triggering efficient charge transport? To address this, we investigate the influence of the organic spacer by selecting different types of R cation in $n = 2$ LD-HPs in the form of $R_2MAPb_2(I_{1-x}Cl_x)_7$ ($x = 0.1$). First, p–i–n perovskite solar cells (PSCs) have been fabricated, showing two contrasting behaviours: a PCE approaching 8% if shorter spacer cations are selected, and a PCE of <1% if longer cations are used. Then, we correlate such device behaviour with LD-HP crystal orientation, combining grazing incidence wide-angle X-ray scattering (GIWAXS), field emission scanning electron microscopy (FESEM) and optical spectroscopy analysis. In synergy with the experimental work, atomistic materials modelling provides design insights into the role of the organic spacer cation and Cl incorporation in directing vertical orientation of LD-HPs, clarifying the intriguing relationship between material structure and device functionality.

Results and discussion

Optical and device characterisation

We processed $R_2MAPb_2(I_{1-x}Cl_x)_7$ ($n = 2$, $x = 0.1$) thin films using a selected library of R cations sharing an aromatic ring and varying in composition and length. As indicated in Fig. 1(a) and S1 (SI), we explored the inclusion of 2-thiophenemethylammonium (TMA^+), 2-thiopheneethylammonium (TEA^+), benzylammonium (BnA^+), and phenethylammonium (PEA^+), where the aromatic core is either a thiophene or a benzene group, while the length is determined by the alkyl chain, comprising either one or two carbon atoms. This choice is driven by the aim to systematically investigate (i) the influence of heteroatom-containing aromatic groups *versus* their purely carbon-based counterparts, and (ii) the effect of R cation size on the resulting thin film orientation. To achieve vertically aligned LD-HP thin films, we incorporated 10% mol^{-1} of Cl to substitute iodide by partially replacing methylammonium iodide (MAI) with methylammonium Cl (MACl), as recently demonstrated by our group in record efficiency 2 eV bandgap PSCs.[16] For all the selected R cations, we obtained $n = 2$ LD-HP thin films with a typical red-orange colour and a bandgap energy of 2 eV, confirming unaltered optical properties, as shown in Fig. 1(b) by UV-Vis absorption spectroscopy.

To directly test the material potential and functionality under working device conditions, we fabricated thin film LD-HP-based solar cells with an inverted (p–i–n) architecture using common protocols,[16] incorporating the selected R cations. Fig. 1(c) shows the device power conversion efficiencies (PCEs), indicating a binary scenario with two very distinct behaviours: the green area stands for working devices, while the red area represents non-working cells. Devices based on TMA^+ and BnA^+ perform well, achieving a PCE approaching 8%, while devices with TEA^+ and PEA^+ show poor device efficiency (PCE $\approx$ 1%). Additionally, devices based on TMA^+ and BnA^+ exhibit good reproducibility. Fig. 1(d) shows the incident photon-to-current efficiency (IPCE) spectra. In terms of magnitude, TMA^+ and BnA^+ devices clearly outperform the TEA^+ and PEA^+ devices at converting incident photons into charge carriers. Specifically, the integrated current density ($J_{integrated}$) for TMA^+ and BnA^+ devices is one order of magnitude higher than TEA^+ and PEA^+ devices (10 over 1 mA cm^{-2}). In terms of spectral dependence, they all show a clear cutoff at 2 eV (580 nm), typical of the $n = 2$ phase, together with the spectral feature characteristic of the $n = 3$ phase at 630 nm and no higher-n LDP phases.[27]

Fig. 1(e–g) show the PV parameters obtained from the current density–voltage (J–V) characteristics, *i.e.*, the short-circuit current density (J_{sc}), open-circuit voltage (V_{oc}), and fill factor (FF). We observe a striking difference between the short- and long-alkyl-chained spacer R cations in J_{sc} and FF, which ultimately results in markedly different PCEs. On the one hand, TMA^+ and BnA^+ exhibit mean J_{sc} values of 9.1 mA cm^{-2} and 7.2 mA cm^{-2} and FFs of 63.7% and 70.4%, respectively. On the other hand, TEA^+ and PEA^+ both show approximately the same J_{sc} and FF of 2 mA cm^{-2} and 40%, respectively. V_{oc} values of the TMA^+ and BnA^+ based devices show improved statistical reproducibility. J–V curves of the top-performing devices from the TMA^+ and BnA^+ series are shown in Fig. S2 (SI).

Based on the PV parameters, the selected R cations can be divided into those that form functional/working materials and those that do not. More specifically, for TMA^+ and BnA^+ cations,

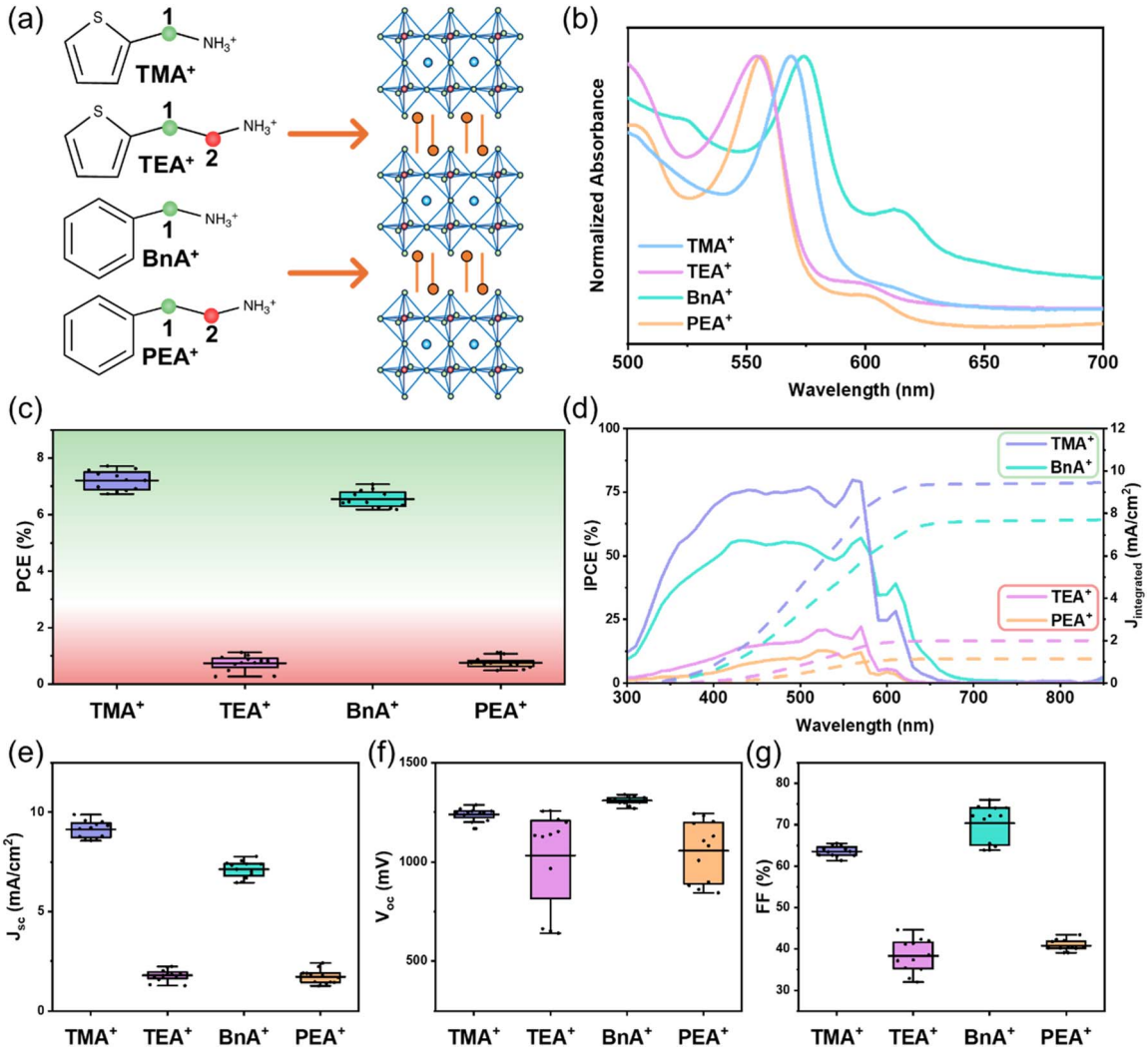

Fig. 1 (a) Schematic illustration of selected R cations to study verticalisation dynamics in $R_2MAPb_2(I_{1-x}Cl_x)_7$ LD-HPs. The R cations are TMA^+ = 2-thiophenemethylammonium, TEA^+ = 2-thiopheneethylammonium, BnA^+ = benzylammonium, and PEA^+ = phenethylammonium, bearing aliphatic chains with one or two carbon atoms. The first carbon atom is highlighted in green and the second in red, emphasizing that the latter is responsible for the performance drop observed in such $n = 2$ LD-HP-based devices. (b) UV-Vis spectra of the $R_2MAPb_2(I_{1-x}Cl_x)_7$ ($x = 0.1$) thin films fabricated with the different R cations. (c) PCE box charts for the $R_2MAPb_2(I_{1-x}Cl_x)_7$-based solar cells fabricated with the different R cations. Statistics of 12 samples are shown. (d) IPCE spectra and $J_{integrated}$ measurements for the $R_2MAPb_2(I_{1-x}Cl_x)_7$-based solar cells fabricated with the different R cations. (e) J_{sc}, (f) V_{oc}, and (g) FF box charts for the $R_2MAPb_2(I_{1-x}Cl_x)_7$-based solar cells fabricated with the different R cations. Sample size is 12.

charge transport and extraction occurring across the inorganic backbone are efficient, as reflected by J_{sc} and FF, while for TEA^+ and PEA^+, they are strongly suppressed. According to the unchanged optical properties, this suggests that the choice of different R cations can decisively impact the crystal orientation of LD-HP thin films, which may favour or impede charge collection. This on–off behaviour in PCE underscores the critical importance of controlling the growth orientation of $n = 2$ LD-HP thin films to achieve efficient PV performance (see also Table S1 (SI) for a comparative overview of reported literature data on 2 eV LD-HP- and 3D-based PSCs). Device stability was evaluated *via* maximum power point tracking (MPPT) to compare Cl-containing TMA^+ and BnA^+ systems (Fig. S3(a) (SI)) and to assess the effect of Cl under operational conditions (Fig. S3(b) (SI)). Both Cl-containing devices exhibit similar stability and are superior to those without Cl, reaching t_{80} after ≈10 000 minutes, which also exceeds the performance reported for single-junction 3D-based 2 eV devices.[16]

Structural orientation analysis

To verify our hypothesis on the LD-HP orientation, we investigated the crystallographic structure and texture of thin films formed by the different R cations using grazing-incidence wide-angle X-ray scattering (GIWAXS) and X-ray diffraction (XRD) techniques. Fig. 2(a–d) show the GIWAXS reciprocal space maps of the studied LD-HP thin films. The diffraction pattern for all investigated samples indicates the presence of $n = 2$ LD-HPs with a peak at $q \sim 0.3$ Å^{-1} for TMA^+ and BnA^+ (shorter spacer cations) and at $q \sim 0.29$ Å^{-1} for TEA^+ and PEA^+ (longer spacer

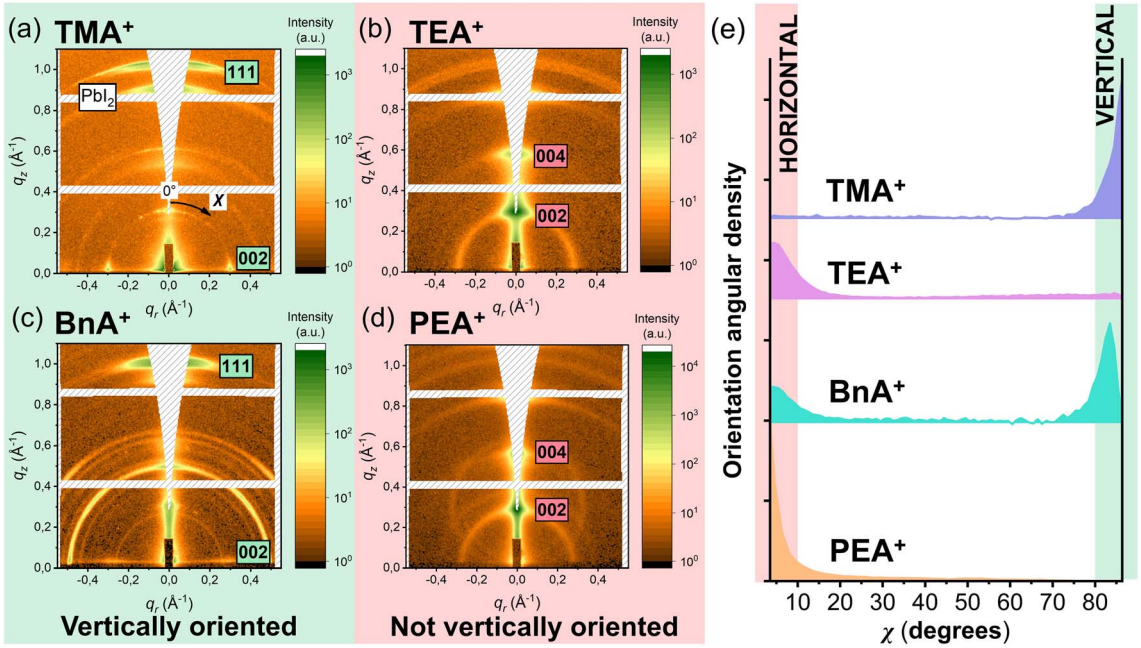

Fig. 2 (a–d) GIWAXS reciprocal space maps of $R_2MAPb_2(I_{1-x}Cl_x)_7$ ($x = 0.1$) thin films fabricated with the different R cations. Thin films with preferential vertical and horizontal orientation are highlighted in green and red frames, respectively. (e) Angular density of the LD-HP orientation calculated from the GIWAXS intensity pattern. The horizontally and vertically oriented phases are highlighted by a color frame in the vicinity of $\chi = 0°$ and 90°, respectively.

cations), corresponding to diffraction from the (002) planes at different orientations. The higher-order diffractions are also present, namely (004) and (111).[28] However, assigning the spatial orientation of the LD-HP directly from the diffraction intensity can be misleading. The GIWAXS reciprocal map captures only a single two-dimensional slice of the three-dimensional reciprocal space, so the total scattering intensity for a particular LD-HP is not provided. To obtain accurate information on texture or plane orientation, the measured intensity has to be rescaled by a correction factor $|\sin(\chi)|$ to account for the angular dependence of the signal.[29]

Fig. 2(e) presents the orientation angular density obtained from the integrated peak intensity along the χ-arc in the GIWAXS reciprocal maps after applying the angular correction (see Fig. 2(a) for the definition of angle χ). It can be seen that mainly two orientations of the LD-HP are present: preferentially vertical in TMA^+ and BnA^+, and predominantly horizontal in TEA^+ and PEA^+ thin films, indicating distinct alignments of the inorganic backbone with respect to the substrate.

The structural differences provide a clear rationale behind the PV performance trends discussed above, underscoring that achieving a proper orientation in LD-HP active layers is critical for attaining high J_{sc} and FF, and thus enhancing PCE, when integrated in a PSC.[23] The phase distribution observed in the various LD-HP thin films directly accounts for the J_{sc} behaviour of the corresponding devices. TEA^+ and PEA^+ thin films, lacking vertically oriented phases, exhibited very low J_{sc}. TMA^+ thin films, with a high degree of vertical alignment, achieved the highest values of J_{sc}. BnA^+ thin films, with only partial vertical alignment, have nevertheless delivered high J_{sc} for $n = 2$ LD-HP-based devices, although slightly lower than that of TMA^+-based PSCs; this is due to the detrimental contribution of the fraction of horizontally oriented domains, which hinder vertical charge transport. These distinct structural features are also confirmed by the presence or absence of the reflection associated with a vertically oriented $n = 2$ LD-HP phase in the XRD patterns shown in Fig. S4 (SI). In particular, a predominant vertical orientation of the inorganic planes occurs only in the TMA^+ and BnA^+ samples, as indicated by the predominance of diffraction peaks relative to the (111) and (220) planes.

Morphology and transient absorption spectroscopy

Fig. 3(a–d) shows the morphological analysis of the cross-section *via* SEM, aimed at understanding potential differences in the thin film structure at the microscale, given its critical impact on charge transport efficiency upon device integration. In line with the previous observations, we find a clear distinction between short- and long-alkyl-chained R cations: TMA^+ and BnA^+ samples exhibit a compact and uniform morphology with large grains, whereas TEA^+ and PEA^+ thin films show smaller and randomly distributed grains, with arbitrary orientation even at a micro-scale, in full agreement with the observed device behaviour.

Different orientations of $n = 2$ LD-HP thin films also manifest in their optical responses, which we investigated using Transient Absorption Spectroscopy (TAS). To probe anisotropy, we specifically monitor the photobleaching (PB) signal under different pump polarisations and sample orientations; see Fig. S5 and S6 (SI) for full spectra and anisotropy data. The investigation of out-of-plane anisotropy involves two pump polarisations (0° and 90°) at both normal incidence and with

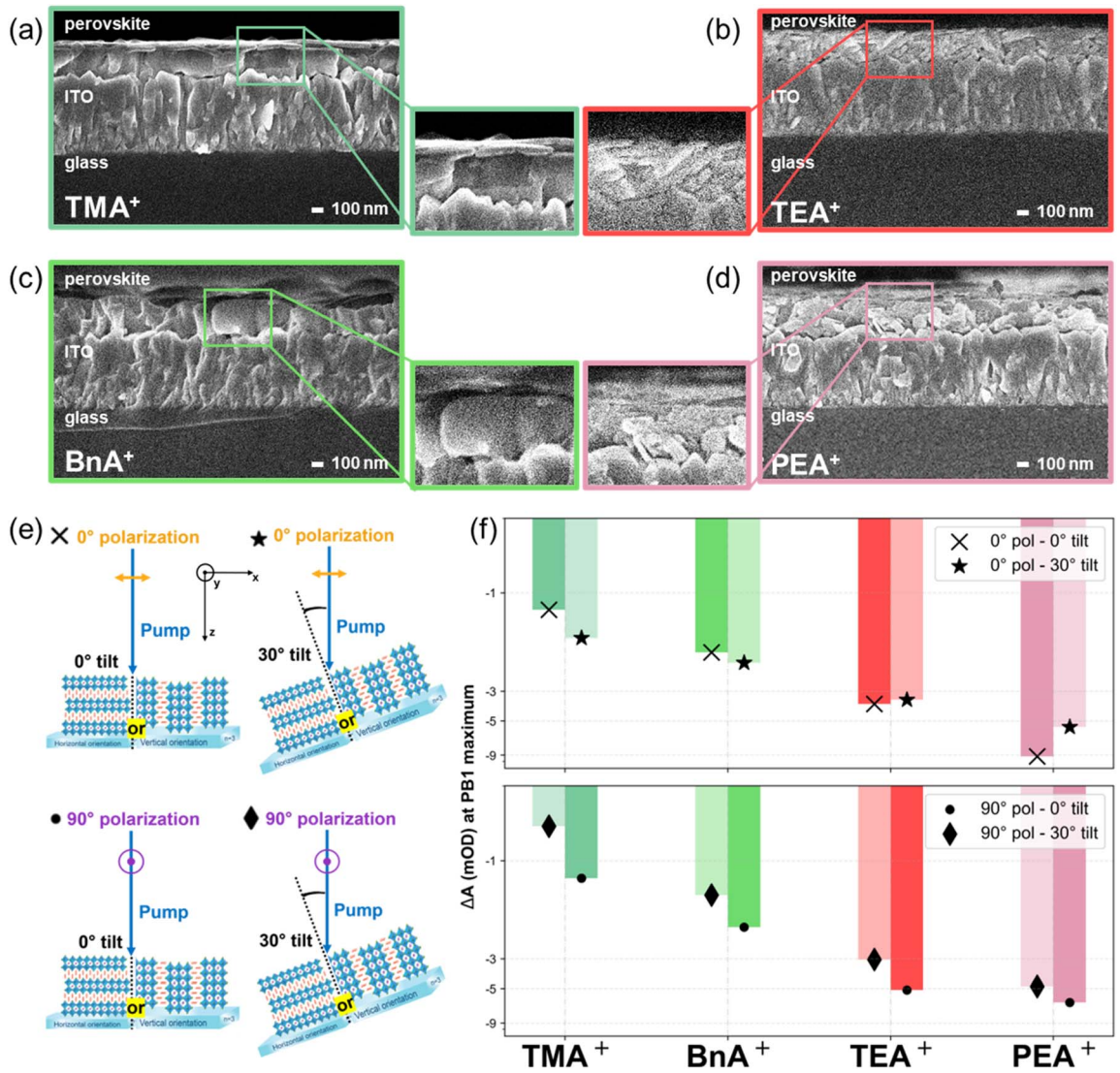

Fig. 3 (a–d) Cross-sectional SEM images of $R_2MAPb_2(I_{1-x}Cl_x)_7$ ($x = 0.1$) thin films fabricated with the different R cations. Deposition was made on glass/ITO substrates. The zoomed-in areas highlight how, in the case of LD-HP thin films with preferential vertical orientation (green boxes), (a) and (c), the thin film exhibits large grains and a uniform morphology, whereas for thin films with preferential horizontal orientation (red boxes), (b) and (d), the thin film displays smaller grains with non-uniform spatial orientation and a high grain boundary density. (e) Graphical illustration of the different setup configurations adopted for the TAS measurement. (f) Photobleaching (PB) intensities from TAS measurements of $R_2MAPb_2(I_{1-x}Cl_x)_7$ ($x = 0.1$) thin films. For each subplot, two setup configurations are compared, as detailed in each panel. In the top (bottom) panel, the tilt angle of the thin film relative to the pump beam is varied from 0° (normal incidence) to 30° (tilted) for each sample type, while keeping 0° (90°) pump polarisation. Comparison of the top and bottom panels gives information about out-of-plane anisotropy, as detailed in the main text.

the sample tilted by 30°, as schematized in Fig. 3(e). At normal incidence, both states are s-polarized, while tilting introduces a p-polarisation component for the 0° pump state only. For the 90° pump polarisation, tilting the sample decreases the PB signal in all thin films, consistent with optical anisotropy arising from the experimental geometry (Fig. 3(f), bottom panel). In contrast, under 0° pump polarisation, the vertically oriented thin films (TMA^+ and BnA^+) exhibit an increased PB signal when tilted (Fig. 3(f), top panel). This increase is attributed to intrinsic structural anisotropy. Tilting the sample introduces an out-of-plane excitation component that more effectively couples with the transition dipole moment of the vertically oriented inorganic layers, an effect strong enough to overcome the optical anisotropy. Conversely, the horizontally oriented thin films (PEA^+ and TEA^+) show a reduced signal when tilted (Fig. 3(f), top panel), as expected from purely optical anisotropy. These results confirm a structural out-of-plane anisotropy in the vertically oriented TMA^+ and BnA^+ samples. In contrast, a similar analysis for in-plane anisotropy, performed by rotating the thin film by 90° in the *xy*-plane (not depicted), did not yield consistent results (Fig. S7 (SI)).

Atomistic insights from materials modelling

To gain a deeper atomistic understanding of directional crystallisation of LD-HPs, we extended our previous *ab initio* modelling studies[16,30,31] to examine how 10% Cl incorporation

affects vertical orientation of the thin films for each R cation. Specifically, we consider (i) the amount and distribution of Cl incorporation, (ii) the effect of Cl on crystal surfaces, and (iii) the possible interfacial energetics arising during crystallisation for the BnA^+-, TMA^+-, PEA^+- and TEA^+-based materials.

We find that in each of the four LD-HPs, Cl incorporation into the bulk is feasible, although the extent depends strongly on the R cation. While Cl inclusion is known to be energetically unfavourable in the 3D $MAPbI_3$ structure,[32,33] low-*n* LD-HPs behave differently. Some Cl can be stably incorporated into the iodide-rich bulk structure, in agreement with our earlier work on LD-HPs showing that Cl incorporation is possible.[16] However, the maximum stable amount of Cl incorporation is always below 9%. Higher levels are only achievable kinetically within the metastable region (Fig. 4(a) and S8 (SI)). Structures with longer-chain spacer cations can incorporate more Cl compared to shorter-chain cations (*i.e.*, TEA^+ 8.2%, PEA^+ 6.5% *versus* TMA^+ 5.2%, BnA^+ 0.8%). These results confirm that bulk Cl incorporation is achievable for all spacer cations, within R cation-dependent bounds. Importantly, smaller R cations, which favour vertical thin film formation (such as BnA^+, TMA^+), incorporate less Cl. As a result, more Cl remains in the precursor solution, where it may contribute to slowing the crystallisation process.[34,35]

In addition to modelling the extent of Cl-incorporation, we probed whether the spatial arrangement of Cl in the bulk varies systematically between preferential vertical (TMA^+ and BnA^+) and horizontal (TEA^+ and PEA^+) thin film orientations. We find that Cl incorporation in TMA^+, TEA^+, and PEA^+ systems has R cation-dependent site preferences: Cl tends to occupy equatorial sites, while in the BnA^+ structure it preferentially occupies axial sites furthest from the spacer cations (Fig. S9 (SI)). This site dependence leads to distinct anisotropic lattice distortions: equatorial substitution contracts the lattice perpendicular to the *c*-axis with compensating expansion along it, whereas axial substitution compresses the *c*-axis. This behaviour is supported experimentally for BnA^+-based thin films, where increasing Cl content shifts the (111) reflections to lower 2θ angles (Fig. S10 (SI)), confirming axial Cl inclusion. For the TMA^+ system, XRD results from our previous study similarly revealed lattice distortions, attributed to equatorial Cl incorporation.[16] However, because both axial (BnA^+) and equatorial (TMA^+) Cl incorporation are compatible with vertical thin film formation,

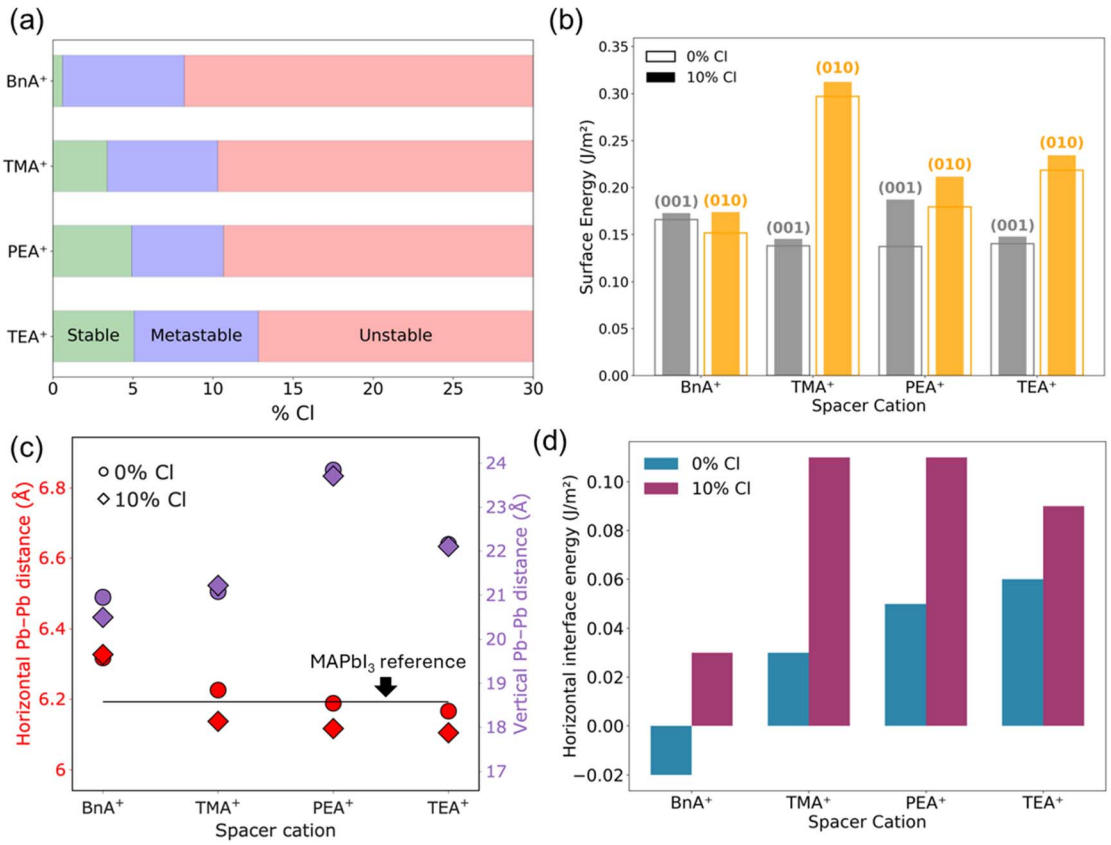

Fig. 4 (a) Simulated Cl incorporation at 400 K as a percentage of total halide-sites in the LD-HP structure. Stable, metastable, and unstable regions are defined by binodal and spinodal points on the free energy curves from generalized quasi-chemical approximation (GQCA) phase diagrams. (b) Surface energies for vertically (010)-terminated and horizontally (001)-terminated surfaces in 0% Cl and 10% Cl-incorporated compositions. (c) Distribution of Pb–Pb distances to quantify lattice mismatch between LD-HP and $MAPbI_3$. Circles represent 0% Cl compositions and diamonds represent 10% Cl systems (red: horizontal distances; purple: vertical distances). (d) Interface energies between horizontal LD-HP and $MAPbI_3$, with and without Cl incorporation in the LD-HP. For all figures (a–d) "0% Cl" and "10% Cl" refer to $R_2MAPb_2(I_{1-x}Cl_x)_7$ $x = 0$ and $x = 0.1$ compositions respectively, where R is the respective spacer cation.

lattice distortions alone cannot account for why only certain spacer cations yield vertical growth.

Since both spacer cations associated with vertical growth (BnA^+ and TMA^+) incorporate comparatively small amounts of Cl into the bulk, the remaining Cl in solution could influence surface energetics and thereby growth orientation.[34] Given that directional crystallisation of LD-HPs can be approximated as a competition between horizontal (001) and vertical (010) surfaces (Fig. S11 (SI)), we calculated the surface energies of these terminations for both pristine and Cl-doped compositions. As shown in Fig. 4(b), Cl incorporation induces only minor changes: the (001) surface remains more stable than the (010) in all cases, and this energetic ordering is preserved with 10% Cl addition. This result shows that the presence of Cl at the surface does not promote vertical growth and cannot explain the experimentally observed thin film orientations.

All the above factors indicate that vertical thin film growth is not straightforward to rationalise in the case of BnA^+-and TMA^+-based structures, suggesting that the nucleation process of these LD-HPs itself may offer an alternative explanation. Previous studies have shown that LD-HPs preferentially nucleate at the air–liquid interface[23,24,36] and evolve from bulk-like high-n phases towards lower-n structures.[37] Our efforts to grow thin films on different substrates support this observation. The directed crystal orientations were achieved across different substrates (Fig. S12 (SI)), indicating that the nucleation might not occur at the substrate–solution interface but top down from the air–liquid interface. In this context, it is the interface energetics between high-n and low-n phases, rather than free surface energetics, that governs the orientation of nucleation and subsequent crystal growth. Here we used bulk $MAPbI_3$ as a representative high-n phase to examine lattice matching and interface energies with each LD-HP composition, as it forms the 3D-like backbone of the thin films under investigation.

First, we examined the lattice strain by comparing the simulated Pb–Pb distances in the LD-HP compositions with bulk $MAPbI_3$ (Fig. 4(c), S13 and S14 (SI)) without explicitly modelling the interfaces, to establish a systematic understanding of strain during LD-HP nucleation. In all pristine compositions, horizontal (a/b plane) Pb–Pb distances (~6.20 Å) lie closer to the $MAPbI_3$ reference values (6.19 Å) than vertical (c-axis) distances, indicating better lattice matching in horizontal orientations. This result agrees with our experimental observations that pristine LD-HPs preferentially crystallize horizontally (Fig. S15 (SI)). Upon 10% Cl incorporation, horizontal Pb–Pb distances increase from the $MAPbI_3$ baseline for all spacer cations except BnA^+, indicating increased strain. Notably, in the BnA^+ system the horizontal distances are maintained while the vertical distances decrease, yielding enhanced vertical compatibility. For TMA^+, the vertical distances are unchanged but the horizontal distances increase, again improving chances of vertical alignment. In contrast, PEA^+ and TEA^+ also show increased horizontal mismatch, but their vertical Pb–Pb distances (23.8 and 22.1 Å) remain substantially offset from the $MAPbI_3$ reference value, providing no indication of favourable vertical growth.

To go beyond the picture of Pb–Pb lattice mismatch, we explicitly modelled LD-HP:$MAPbI_3$ horizontal interfaces and computed their interface energies (Fig. 4(d)). For $MAPbI_3$ we consider the stable and well-studied (001) PbI-terminated surface.[38,39] Consistent with the lattice matching analysis, Cl incorporation systematically increases the horizontal interface energy across all systems (more for TMA^+ and BnA^+), making horizontal growth less favourable.

Overall, our systematic atomistic modelling analysis indicates that Cl incorporation in $n = 2$ LD-HPs is limited and strongly spacer cation-dependent. Larger spacer cations (TEA^+ and PEA^+) accommodate higher levels of Cl than smaller cations (TMA^+ and BnA^+). For TMA^+ and BnA^+, this result implies that a larger fraction of Cl remains in the precursor solution, which may contribute to slower crystallisation kinetics based on previous reports on Cl-assisted perovskite growth.[40,41] Excess Cl does not lower the energy of vertically oriented surfaces relative to horizontal ones, ruling out favourable surface energetics as the origin of vertical crystallisation. Instead, lattice strain and interface energetics reveal that Cl incorporation increases the penalty for horizontal interfaces, thereby suppressing horizontal growth and shifting the balance towards vertical crystallisation for TMA^+ and BnA^+, but not for TEA^+ or PEA^+.

Conclusion

In this work, we have systematically investigated how chloride incorporation and the structure of organic spacer cations (R) govern the crystal orientation and photovoltaic performance of $n = 2$ $R_2MAPb_2(I_{1-x}Cl_x)_7$ ($x = 0.1$) low-dimensional halide perovskites (LD-HPs). Integration of these LD-HP thin films into p–i–n perovskite solar cells revealed two distinct behaviours: highly efficient devices (2 eV bandgap) employing short R cations (TMA^+ and BnA^+), and poorly-efficient devices based on long cations (TEA^+ and PEA^+). Structural and morphological characterisation showed that the highly efficient devices exhibit preferential out-of-plane orientation of the inorganic framework and improved morphology, both of which enhance vertical charge transport and collection. Transient absorption spectroscopy further confirmed vertically aligned domains as the dominant growth mode in efficient devices.

Analysis of systematic trends from *ab initio* atomistic modelling revealed that Cl incorporation is strongly spacer cation dependent: smaller cations (TMA^+ and BnA^+) incorporate only modest amounts of Cl, leaving excess chloride in solution likely to slow the crystallisation kinetics. Surface energy results exclude direct stabilisation of vertical facets by Cl. However, lattice strain and LD-HP:$MAPbI_3$ interface simulations reveal that Cl incorporation increases the energetic penalty for horizontal growth most strongly in TMA^+ and BnA^+ systems, favouring their vertical crystallisation.

Beyond the mechanistic understanding, this work demonstrates PCEs approaching 8% for purely $n = 2$ LD-HP-based devices, among the highest reported for such wide-bandgap materials. These findings highlight the importance of controlling crystal orientation through spacer cation design and chloride incorporation, providing a pathway towards high-

performance wide-bandgap perovskite photovoltaic applications.

Experimental

Materials

Acetone (≥99.8%) and bathocuproine (BCP, sublimed grade, 99.99% purity) were purchased from Sigma Aldrich. Isopropanol (IPA, extra dry, ≥99.8%), toluene (TOL, extra dry, 99.8%), chloroform (CF, extra dry, 99.8%) and *N*,*N*-dimethylformamide (DMF, extra dry, 99.8%) were purchased from Acros Organics. Lead iodide (PbI_2,>98.0%), lead chloride ($PbCl_2$, 99.0%) and (2-(3,6-dimethoxy-9*H*-carbazol-9-yl)ethyl) phosphonic acid (MeO-2PACz) were purchased from TCI. Methylammonium iodide (MAI, >99.99%), methylammonium chloride (MACl, >99.99%), 2-thiophenemethylammonium iodide (TMAI), 2-thiopheneethylammonium iodide (TEAI), benzylammonium iodide (BnAI), and phenethylammonium iodide (PEAI) were purchased from GreatCell Solar Materials. (6,6)-Phenyl C61 butyric acid methyl ester (PCBM, >99.5%) was purchased from Lumtec. All solutions were prepared in an Ar-filled glovebox, while the deposition of each layer of the PSC was performed in an N_2-filled glovebox.

Device fabrication

For the fabrication of LD-HP-based PSCs, indium tin oxide (ITO)-coated glass substrates (purchased from Yingkou Shangneng Photoelectric material Co., Ltd) were consecutively cleaned in acetone and IPA by ultrasonication for 15 min for each solvent. Substrates were dried under N_2 airflow and treated with O_2 plasma for 10 min. MeO-2PACz was dissolved in ethanol (0.335 mg mL^{-1}) and 40 μL were spin-coated onto ITO/glass substrates at 3000 rpm for 30 s and annealed at 100 °C for 10 min. The precursor solution (0.7 M) for the $R_2MAPb_2(I_{1-x}Cl_x)_7$ ($x = 0.1$) LD-HPs was prepared by mixing a stoichiometric ratio of PbI_2, MAI, MACl, and the selected R-cation, namely thiophenemethylammonium (TMA^+), thiopheneethylammonium (TEA^+), benzylammonium (BnA^+), or phenylethylammonium (PEA^+) iodide salt powders. Specifically, 70 mol% of MAI was replaced by MACl, without changing the total stoichiometric amount of MA in the solution. The precursor solution for pristine $R_2MAPb_2I_7$ LD-HPs was prepared by mixing stoichiometric amounts of all the aforementioned precursors, except MACl. After complete dissolution, the solution was subjected to a thermal annealing step of 2 h at 60 °C. 30 μL of the final solution was deposited on the MeO-2PACz-coated substrates and spin-coated with a single-step spin coating procedure at 4000 rpm, with an acceleration of 2000 rpm s^{-1} for 40 s. 120 μl of TOL was dropped onto the spinning substrate 20 s before the end of the programme for the antisolvent procedure. Subsequently, the samples were annealed at 100 °C for 30 min. To fabricate the ETL, PCBM was dissolved in CF (15 mg mL^{-1}) and 20 μL of the solution was spin-coated at 2000 rpm for 20 s onto the perovskite layer. To prevent the diffusion of the metal contact inside the perovskite, 50 μL of 1 mg per mL solution of BCP in IPA was deposited on PCBM. Finally, 80 nm of Ag was thermally evaporated on the device with a shadow mask of 0.0825 cm^2 area, producing devices of 0.045 cm^2 active area as a result of the overlapping area between the ITO and the metal contact. The evaporation speed was adjusted to 0.01 nm s^{-1} for the first 5 nm, 0.02 nm s^{-1} from 5 to 15 nm, and 0.06 nm s^{-1} for the rest of the procedure. For the fabrication of LD-HP thin films, glass substrates were cleaned using the same procedure applied to the ITO-coated glass substrates. The LD-HP layer was fabricated following the same procedure employed to prepare the PSC active layer. For all depositions, a vacuum-based chuck was used.

Current density–voltage characteristics

Current density–voltage (*J*–*V*) characteristics of the produced PSCs were carried out using a Keithley 2400 source meter and an Abet solar simulator. The simulated 1 sun AM1.5G illumination was calibrated using a certified Si reference cell (Open RR-1002, KG5 window). The devices were measured in an ambient atmosphere, at room temperature, in reverse and forward scan in the 0–1.5 V voltage range at 130 mV s^{-1} scan rate. During measurement, a metal shadow mask with an aperture area of 0.03 cm^2 was used. Measurements were performed on devices fabricated within the same batch.

Incident photon-to-current efficiency

Incident photon-to-current efficiency (IPCE) measurements were performed in the dark, with background illumination removed, using a Cicci Research Arkeo steady-state testing module. The wavelength scan range was set between 300 and 900 nm with a scan step of 10 nm.

UV-Vis absorption

The UV-Vis absorption spectra of LD-HP thin films were collected using a UV-NIR spectrophotometer from PerkinElmer (Lambda 1050+).

Grazing-incident wide-angle X-ray scattering

Grazing-incidence wide-angle X-ray scattering (GIWAXS) reciprocal space maps were obtained using a custom-built laboratory system equipped with a MetalJet X-ray source (Excillum) operating at 9.25 keV ($\lambda = 1.34$ Å). The incident angle of the X-ray beam was set to 0.2°. Diffraction patterns were recorded using a two-dimensional detector Pilatus 300 K (Dectris). All GIWAXS measurements were conducted under vacuum to minimize X-ray scattering from air, which would otherwise reduce the signal-to-noise ratio of diffractions close to the direct and reflected X-ray beams, particularly those originating from the 2D perovskite structures.

X-ray diffraction

X-ray diffraction (XRD) patterns of LD-HP thin films were acquired using a Bruker D2 X-ray diffractometer coupled with a Cu X-ray tube ($\lambda = 1.5418$, 300 W, 30 kV) and a Lynxeye (1D mode) detector. Measurements were performed adopting a 0.02° step size and a 0.5 step s^{-1} scan rate.

Field emission scanning electron microscopy

Morphological characterisation was performed using a Field Emission Scanning Electron Microscope (FESEM, JEOL JSM-7600F, 5 kV, and 10 mA).

Transient absorption spectroscopy

Transient absorption spectroscopy measurements were performed on a commercial ultrafast pump-probe setup (HARPIA-TA, Light Conversion) equipped with an amplified femtosecond Yb:YAG laser with 120 fs pulse duration and 50 kHz repetition rate for seeding (PHAROS, Light Conversion). An optical parametric amplifier (ORPHEUS, Light Conversion) was employed to generate the pump beam. The pump central wavelength was kept at 560 nm for all experiments; the pump power at the sample plane was set at 50 μW and measured before and after each measurement with a Si power meter (Thorlabs). To conduct the pump-probe experiment, a broadband (550–920 nm) white-light probe beam was generated *via* supercontinuum generation from a 1 cm thick sapphire crystal and delayed through a motorized delay line. The signal was detected *via* a high-performance spectrograph (Andor Kymera, Oxford Instruments) equipped with an 850 nm blazed visible grating. Samples were mounted on a 3D-printed custom sample holder that allows rotation around the vertical axis, normal to the optical table plane.

Statistical analysis

OriginPro 2018 software was employed to perform statistical analysis. For photovoltaic parameters, dataset was arranged in box charts, where whiskers limit the 1.5 interquartile range, the box identifies the 25th and 75th percentiles and the horizontal line represents the average value. Sample size is reported for each analysis.

Density functional theory (DFT) calculations

All first-principles calculations were performed using VASP[42,43] within the projector augmented-wave (PAW) method, employing standard VASP PAW pseudopotentials for all elements. Exchange–correlation effects were treated using the Perdew–Burke–Ernzerhof (PBE) functional,[44] together with Grimme's DFT-D3 dispersion corrections.[45] Plane-wave cutoffs of 600 eV and 500 eV were used for bulk and surface models, respectively, with Γ-centred Monkhorst–Pack sampling (KSPACING = 0.40 $Å^{-1}$ for bulk, 0.35 $Å^{-1}$ for surfaces). The electronic self-consistent field convergence criterion was set to 10^{-6} eV for all calculations. Geometry optimisations were performed using the conjugate-gradient algorithm until all residual forces were below 0.01 eV $Å^{-1}$. Dipole corrections were applied in all surface calculations along the direction perpendicular to the surface to eliminate artificial electrostatic interactions arising from the periodic boundary conditions.[46,47]

Machine learning interatomic potential (MLIP)

To efficiently explore halide mixing and configurational disorder beyond the reach of DFT, an MLIP model based on the message-passing atomic cluster expansion (MACE) framework[48] was developed. The model architecture and active-learning protocol were adapted from a previously reported LD-HP potential[49] and extended to include sulphur-containing species (TMA^+ and TEA^+). Comprehensive details of the LD-HP structures, MLIP training, chloride sampling strategy, and surface/interface models are available in the SI.

Author contributions

Conceptualisation: A. S., T. F. L., V., M. S. I., and G. G. Investigation: A. S., T. F. L., N. M., R. S., V., L. M., H. A. D., and R. P. Writing—original draft: A.S., R. P., T. F. L., V., and G. G. Writing—review & editing: A. S., T. F. L., N. M., R. S., V., L. M., H. A. D., R. P., A. B. M. S. I., and G. G. Supervision: A. B., P. S., M. S. I., and G. G.

Conflicts of interest

There are no conflicts to declare.

Data availability

All input structures, machine learning potential training data, and analysis scripts used in this study are available in a dedicated GitHub repository (https://github.com/TFL600/LD-HP_crystal_orientation). The repository will be publicly available on Zenodo (DOI: https://doi.org/10.5281/zenodo.17376510) upon publication.

All the other data that support the findings of this study are available from the corresponding authors upon request.

Supplementary information (SI) is available. See DOI: https://doi.org/10.1039/d6el00006a.

Acknowledgements

The authors are thankful to the Ministero dell'Università e della Ricerca (MUR), University of Pavia through the program "Dipartimenti di Eccellenza 2023–2027". G. G. acknowledges the "ELOW-DI" project that received funding from the European Research Council (ERC) Consolidator Grant 2025 under the European Union's Horizon Europe research and innovation programme (Grant Agreement no. 101171012). G. G. and A. S. acknowledge the GOPV project (CSEAA_00011), which received funds from Bando Ricerca di Sistema—CSEA—TIPO A Piano triennale 2019–2021 Decreto direttoriale 27 Ottobre 2021 del Ministero della Transizione Ecologica. The authors acknowledge further the financial support of projects IMPULZ (IM-2023-82), APVV-21-0297, APVV-24-0321, 2023/727/PVKSC, OSCARS project no.101129751, and ITMS project code 313021T081. M. S. I. and T. F. L. acknowledge the Department of Materials at the University of Oxford for a DTP studentship. M. S. I. and V. acknowledge the Engineering and Physical Sciences Research Council (EPSRC) Programme Grant (EP/X038777/1) for a post-doctoral fellowship. The authors are grateful to the UK's HEC Materials Chemistry Consortium (EP/X035859/1) for the use of the ARCHER2 high-performance computing facilities and

would also like to acknowledge the use of the University of Oxford Advanced Research Computing (ARC) facility in carrying out this work (https://doi.org/10.5281/zenodo.22558). A. B. would like to acknowledge the AcRF Tier 1 grants from MOE (RG84/24 and RS18/24), Singapore.

References

1 Y. Tong, A. Najar, L. Wang, L. Liu, M. Du, J. Yang, J. Li, K. Wang and S. Frank, *Adv. Sci.*, 2022, **9**, 2105085.
2 I. Mathews, S. N. Kantareddy, T. Buonassisi and I. M. Peters, *Joule*, 2019, **3**, 1415–1426.
3 A. Chakraborty, G. Lucarelli, J. Xu, Z. Skafi, S. Castro-Hermosa, A. B. Kaveramma, R. G. Balakrishna and T. M. Brown, *Nano Energy*, 2024, **128**, 109932.
4 C. J. Traverse, R. Pandey, M. C. Barr and R. R. Lunt, *Nat. Energy*, 2017, **2**, 849–860.
5 A. R. Groves, *Nat. Synth.*, 2025, **4**, 1021.
6 Y. Zhang, R. Wang and Z. Tan, *J. Mater. Chem. A*, 2023, **11**, 11607–11636.
7 S. Sahayaraj, E. Radicchi, M. Ziółek, M. Ścigaj, M. Tamulewicz-Szwajkowska, J. Serafińczuk, F. De Angelis and K. Wojciechowski, *J. Mater. Chem. A*, 2021, **9**, 9175–9190.
8 S. Peng, J. Liu, C. Liang, G. Chen, Y. Shi, Z. Miao, W. Liang, T. Zhang, Y. Xie, Y. Zhang, Y. Song and P. Li, *Joule*, 2025, **9**, 102079.
9 F. Toniolo, L. Pancini, A. Oranskaia, N. Mrkyvkova, P. Siffalovic, R. Pallotta, M. Degani, F. Doria, U. Schwingenschlögl and G. Grancini, *Sol. RRL*, 2025, e202500582.
10 M. Degani, R. Pallotta, G. Pica, M. Karimipour, A. Mirabelli, K. Frohna, M. Anaya, T. Xu, C. Q. Ma, S. D. Stranks, M. L. Cantù and G. Grancini, *Adv. Energy Mater.*, 2025, **15**, 2404469.
11 F. Faini, V. Larini, A. Scardina and G. Grancini, *MRS Bull.*, 2024, **49**, 1059–1069.
12 G. Grancini and M. K. Nazeeruddin, *Nat. Rev. Mater.*, 2019, **4**, 4–22.
13 J. Hou, W. Li, H. Zhang, S. Sidhik, J. Fletcher, I. Metcalf, S. B. Anantharaman, X. Shuai, A. Mishra, J. C. Blancon, C. Katan, D. Jariwala, J. Even, M. G. Kanatzidis and A. D. Mohite, *Nat. Synth.*, 2024, **3**, 265–275.
14 X. Zhao, J. Li, J. Cheng, X. Liu and X. Zhao, *Front. Energy*, 2025, 1–23.
15 M. G. D. Guaita, R. Szostak, F. M. C. da Silva, Z. Feng, L. Scalon, V. C. Teixeira, T. Kodalle, C. M. Sutter-Fella, S. S. Jang, H. C. N. Tolentino and A. F. Nogueira, *Sol. RRL*, 2025, **9**, 2500404.
16 A. Zanetta, V. Larini, Vikram, F. Toniolo, B. Vishal, K. A. Elmestekawy, J. Du, A. Scardina, F. Faini, G. Pica, V. Pirota, M. Pitaro, S. Marras, C. Ding, B. K. Yildirim, M. Babics, E. Ugur, E. Aydin, C. Q. Ma, F. Doria, M. A. Loi, M. De Bastiani, L. M. Herz, G. Portale, S. De Wolf, M. S. Islam and G. Grancini, *Nat. Commun.*, 2024, **15**, 1–10.
17 P. Liu, N. Han, W. Wang, R. Ran, W. Zhou and Z. Shao, *Adv. Mater.*, 2021, **33**, 2002582.
18 A. Z. Chen, M. Shiu, J. H. Ma, M. R. Alpert, D. Zhang, B. J. Foley, D. M. Smilgies, S. H. Lee and J. J. Choi, *Nat. Commun.*, 2018, **9**, 1–7.
19 A. Caiazzo, R. A. J. Janssen, A. Caiazzo and R. A. J. Janssen, *Adv. Energy Mater.*, 2022, **12**, 2202830.
20 H. Tsai, W. Nie, J. C. Blancon, C. C. Stoumpos, R. Asadpour, B. Harutyunyan, A. J. Neukirch, R. Verduzco, J. J. Crochet, S. Tretiak, L. Pedesseau, J. Even, M. A. Alam, G. Gupta, J. Lou, P. M. Ajayan, M. J. Bedzyk, M. G. Kanatzidis and A. D. Mohite, *Nature*, 2016, **536**, 312–317.
21 T. Yue, K. Li, X. Li, N. Ahmad, H. Kang, Q. Cheng, Y. Zhang, Y. Yue, Y. Jing, B. Wang, S. Li, J. Chen, G. Huang, Y. Li, Z. Fu, T. Wu, S. U. Zafar, L. Zhu, H. Zhou and Y. Zhang, *ACS Nano*, 2023, **17**, 14632–14643.
22 D. H. Cao, C. C. Stoumpos, O. K. Farha, J. T. Hupp and M. G. Kanatzidis, *J. Am. Chem. Soc.*, 2015, **137**, 7843–7850.
23 J. Wang, S. Luo, Y. Lin, Y. Chen, Y. Deng, Z. Li, K. Meng, G. Chen, T. Huang, S. Xiao, H. Huang, C. Zhou, L. Ding, J. He, J. Huang and Y. Yuan, *Nat. Commun.*, 2020, **11**, 1–9.
24 Y. Lin, Y. Fang, J. Zhao, Y. Shao, S. J. Stuard, M. M. Nahid, H. Ade, Q. Wang, J. E. Shield, N. Zhou, A. M. Moran and J. Huang, *Nat. Commun.*, 2019, **10**, 1–11.
25 R. Jiang, T. Tian, B. Ke, Z. Kou, P. Müller-Buschbaum, F. Huang, Y. B. Cheng and T. Bu, *Next Mater.*, 2023, **1**, 100044.
26 K. Wang, C. Wu, D. Yang, Y. Jiang and S. Priya, *ACS Nano*, 2018, **12**, 4919–4929.
27 S. Pal and S. Uma, *Ceram. Int.*, 2024, **50**, 31540–31547.
28 E. S. Vasileiadou, X. Jiang, M. Kepenekian, J. Even, M. C. De Siena, V. V. Klepov, D. Friedrich, I. Spanopoulos, Q. Tu, I. S. Tajuddin, E. A. Weiss and M. G. Kanatzidis, *J. Am. Chem. Soc.*, 2022, **144**, 6390–6409.
29 J. A. Steele, E. Solano, D. Hardy, D. Dayton, D. Ladd, K. White, P. Chen, J. Hou, H. Huang, R. A. Saha, L. Wang, F. Gao, J. Hofkens, M. B. J. Roeffaers, D. Chernyshov and M. F. Toney, *Adv. Energy Mater.*, 2023, **13**, 2300760.
30 N. Zibouche and M. S. Islam, *ACS Appl. Mater. Interfaces*, 2020, **12**, 15328–15337.
31 Y. H. Lin, Vikram, F. Yang, X. L. Cao, A. Dasgupta, R. D. J. Oliver, A. M. Ulatowski, M. M. McCarthy, X. Shen, Q. Yuan, M. G. Christoforo, F. S. Y. Yeung, M. B. Johnston, N. K. Noel, L. M. Herz, M. S. Islam and H. J. Snaith, *Science*, 2024, **384**, 767–775.
32 M. I. Dar, N. Arora, P. Gao, S. Ahmad, M. Grätzel and M. K. Nazeeruddin, *Nano Lett.*, 2014, **14**, 6991–6996.
33 R. Pallotta, F. Faini, F. Toniolo, V. Larini, M. Schmidt, S. Marras, G. Pica, S. Cavalli, S. Mattioni, L. E. Hueso, M. Degani, B. Martín-García, B. Ehrler and G. Grancini, *Joule*, 2025, **9**(6), 101964.
34 Y. Zhao and K. Zhu, *J. Phys. Chem. C*, 2014, **118**, 9412–9418.
35 R. Pallotta, S. Cavalli, M. Degani and G. Grancini, *Small Struct.*, 2024, **5**, 2300448.
36 B. Chen, K. Meng, Z. Qiao, Y. Zhai, R. Yu, Z. Fang, P. Yan, M. Xiao, L. Pan, L. Zheng, K. Cao and G. Chen, *Adv. Mater.*, 2024, **36**, 2312054.
37 F. Zheng, S. Rubanov, C. Hall, J. Liu, M. Gao, T. A. Smith, D. Angmo, K. P. Ghiggino, F. Zheng, C. Hall, T. A. Smith,

K. P. Ghiggino, M. Gao, D. Angmo, S. Rubanov and J. Liu, *Adv. Mater. Interfaces*, 2025, **12**, 2401012.
38 J. Xue, R. Wang and Y. Yang, *Nat. Rev. Mater.*, 2020, **5**, 809–827.
39 J. Haruyama, K. Sodeyama, L. Han and Y. Tateyama, *J. Phys. Chem. Lett.*, 2014, **5**, 2903–2909.
40 Y. M. Xie, Q. Xue and H. L. Yip, *Adv. Energy Mater.*, 2021, **11**, 2100784.
41 T. Kodalle, M. M. Byranvand, M. Goudreau, C. Das, R. Roy, M. Kot, S. Briesenick, M. Zohdi, M. Rai, N. Tamura, J. I. Flege, W. Hempel, C. M. Sutter-Fella and M. Saliba, *Adv. Mater.*, 2024, **36**, 2309154.
42 G. Kresse and J. Hafner, *Phys. Rev. B: Condens. Matter Mater. Phys.*, 1993, **47**, 558.
43 G. Kresse and J. Furthmüller, *Comput. Mater. Sci.*, 1996, **6**, 15–50.
44 J. P. Perdew, K. Burke and M. Ernzerhof, *Phys. Rev. Lett.*, 1996, **77**, 3865.
45 S. Grimme, J. Antony, S. Ehrlich and H. Krieg, *J. Chem. Phys.*, 2010, **132**(15), 154104.
46 J. Neugebauer and M. Scheffler, *Phys. Rev. B:Condens. Matter Mater. Phys.*, 1992, **46**, 16067.
47 G. Makov and M. C. Payne, *Phys. Rev. B:Condens. Matter Mater. Phys.*, 1995, **51**, 4014.
48 I. Batatia, S. Batzner, D. P. Kovács, A. Musaelian, G. N. C. Simm, R. Drautz, C. Ortner, B. Kozinsky and G. Csányi, *Nat. Mach. Intell.*, 2025, **7**, 56–67.
49 N. Karimitari, W. J. Baldwin, E. W. Muller, Z. J. L. Bare, W. J. Kennedy, G. Csányi and C. Sutton, *J. Am. Chem. Soc.*, 2024, **146**, 27392–27404.